A high-resolution, time-variable afterslip model for the 2010 Maule Mw = 8.8, Chile megathrust earthquake

CrossMark

Jonathan Bedford [a,*], Marcos Moreno [a], Juan Carlos Baez [b], Dietrich Lange [c], Frederik Tilmann [a,d], Matthias Rosenau [a], Oliver Heidbach [a], Onno Oncken [a], Mitja Bartsch [a], Andreas Rietbrock [e], Andrés Tassara [b], Michael Bevis [f], Christophe Vigny [g]

[a] GFZ Potsdam, Germany
[b] Universidad de Concepción, Chile
[c] GEOMAR, Helmholtz-Zentrum für Ozeanforschung Kiel, Germany
[d] Freie Universität Berlin, Germany
[e] University of Liverpool, UK
[f] Ohio State University, USA
[g] Laboratoire de Géologie de l'ENS, UMR 8538 du CNRS, Paris, France

ARTICLE INFO

ABSTRACT

The excellent spatial coverage of continuous GPS stations in the region affected by the Maule Mw = 8.8 2010 earthquake, combined with the proximity of the coast to the seismogenic zone, allows us to model megathrust afterslip on the plate interface with unprecedented detail. We invert post-seismic observations from continuous GPS sites to derive a time-variable model of the first 420 d of afterslip. We also invert co-seismic GPS displacements to create a new co-seismic slip model. The afterslip pattern appears to be transient and non-stationary, with the cumulative afterslip pattern being formed from afterslip pulses. Changes in static stress on the plate interface from the co- and post-seismic slip cannot solely explain the aftershock patterns, suggesting that another process – perhaps fluid related – is controlling the lower magnitude aftershocks. We use aftershock data to quantify the seismic coupling distribution during the post-seismic phase. Comparison of the post-seismic behaviour to interseismic locking suggests that highly locked regions do not necessarily behave as rate-weakening in the post-seismic period. By comparing the inter-seismic locking, co-seismic slip, afterslip, and aftershocks we attempt to classify the heterogeneous frictional behaviour of the plate interface.

© 2013 Elsevier B.V. All rights reserved.

1. Introduction

The period of time during which the subduction zone relaxes the stress induced by a megathrust earthquake is known as the post-seismic, which, depending on magnitude, can last for years or even decades (e.g., Hu et al., 2004; Wang et al., 2012). The post-seismic period presents an excellent opportunity to study subduction zone physics not only because the surface velocity is transient and much larger than before the earthquake, but also because it is accompanied by an increase in seismic activity that shows a similar time decay to the post-seismic surface displacements (Hsu et al., 2006). Moreover, the transient character of the induced deformation allows testing of the time-dependent rheology of the Earth. However, interpreting post-seismic deformation is inherently non-unique and multiple physical mechanisms can explain the post-seismic surface displacements (e.g., Freed et al., 2006; Hergert and Heidbach, 2006; Hu and Wang, 2012). Proposed primary mechanisms of stress relaxation following large earthquakes are afterslip (Hsu et al., 2006; Miyazaki et al., 2004; Perfettini et al., 2010), poro-elastic rebound (Wang, 2000; Hughes et al., 2010), and viscoelastic relaxation of stress (Rundle, 1978; Hu et al., 2004; Hergert and Heidbach, 2006). Rapidly decaying deformation in the near-field of the rupture (lasting for days to 1–2 yr) is generally attributed to afterslip (Hsu et al., 2006), which is characterized by aseismic slip on the plate interface surrounding the rupture as induced by co-seismic stress changes (e.g., Marone et al., 1991). Afterslip has been inferred to be an important mechanism following recent great earthquakes (e.g., Ozawa et al., 2011; Vigny et al., 2011; Hu and Wang, 2012) and its distribution has been used to infer the frictional properties of the megathrust (e.g., Miyazaki et al., 2004; Marone, 1998) and to investigate the trigger mechanism of aftershocks (Helmstetter and Shaw, 2009). The increased coverage of modern geodetic measurements allows us to observe the surface deformation field on finer spatial and temporal scales, adding further constraints to our models of post-seismic processes.
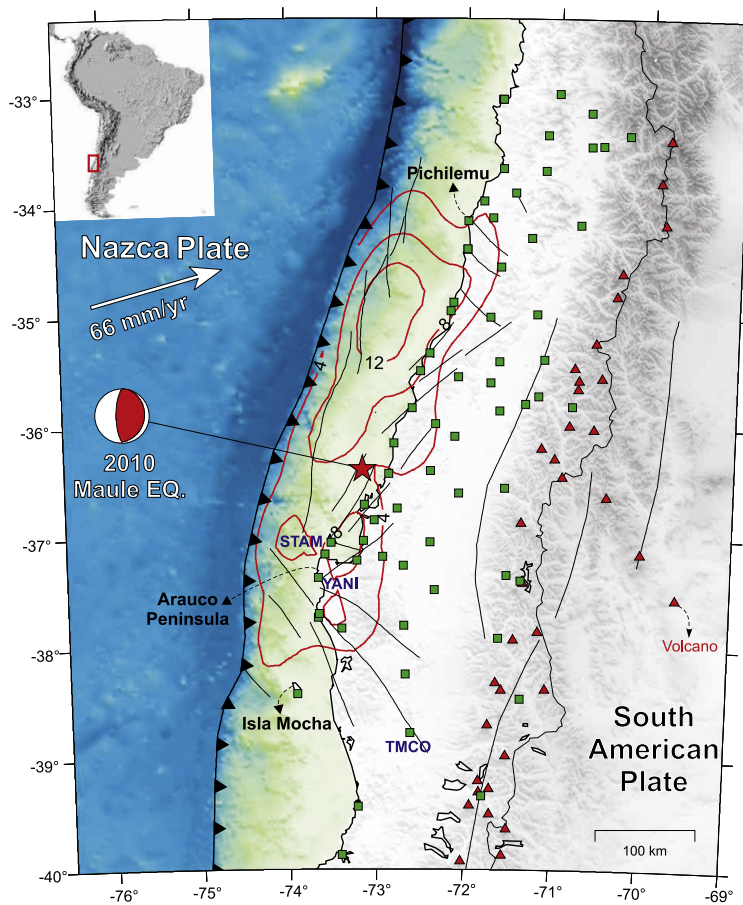
* Corresponding author.

Fig. 1. Tectonic setting for the Maule 2010 subduction earthquake. Green squares indicate locations of continuous GPS stations. Co-seismic slip contours of 4 m, 8 m, and 12 m are plotted in red. Mainshock hypocentre is given by the red star (Vigny et al., 2011) and focal mechanism from the gCMT catalogue is shown. Crustal faults are indicated with black lines. Red triangles indicate Quaternary volcanoes. (For interpretation of the references to colour in this figure, the reader is referred to the web version of this article.)

In this paper we will model the afterslip on the plate interface using the excellent spatio-temporal coverage of continuous GPS (cGPS) in the region of the great (Mw = 8.8) Maule, Chile earthquake of February 27th 2010. While we recognize that other physical processes are contributing to the surface deformation field, we assume afterslip to be the principal dominant contribution to the early post-seismic surface deformation pattern. This assumption is supported by the dominance of plate interface aftershocks in most of the rupture zone (e.g. Lange et al., 2012; Rietbrock et al., 2012; Agurto et al., 2012). Deviations of the predicted (i.e. purely elastic) surface deformation from observed deformation is reasonably attributed to and discussed in the framework of poro-elastic effects, viscoelastic stress relaxation as well as crustal faulting.

In previous studies investigating the spatio-temporal evolution of afterslip (Segall et al., 2000; Miyazaki et al., 2004; Hsu et al., 2006, 2007) the spatial afterslip pattern was mostly not seen to significantly vary with time, i.e. it appeared stationary. However, these models lacked spatial resolution due to either the distance of cGPS stations from the slipping area (Ozawa et al., 2011), or because only very few cGPS stations were available to constrain the model. Our afterslip model of the Maule 2010 earthquake highlights the transient and non-stationary character of afterslip in subduction megathrust settings and shows in detail how the afterslip varied in time and space during the first 14 months. We use our spatio-temporal model to distinguish different frictional behaviour at different regions of the plate interface, and discuss the implications for our understanding of the inter- and co-seismic behaviour of the Maule subduction segment.

The Mw = 8.8 Maule 2010 earthquake ruptured a 500 km long segment of the central Chile Forearc due to the subduction of the Nazca Plate beneath South America (Fig. 1). It occurred on a mature seismic gap, which presented a high degree of plate locking in the decade preceding the event (Ruegg et al., 2009; Moreno et al., 2010; Métois et al., 2012). Strong motion in the near-field (shaking), tsunami run-up and inundation, as well as coastal uplift patterns show similarities to an earthquake in 1835 (Darwin, 1851), suggesting that both events ruptured an analogous segment of the plate boundary (Moreno et al., 2012). Slip peaked at 16 m and back projection of teleseismic waveforms suggest a bilateral propagation of the rupture from the centrally located epicentre (Kiser and Ishii, 2011; Wang and Mori, 2011). There have been various models of co-seismic slip which have improved in resolution as more data have become available (e.g. Delouis et al., 2010; Vigny et al., 2011; Pollitz et al., 2011; Lorito et al., 2011; Moreno et al., 2012). We compare our afterslip model with a co-seismic slip model obtained from inversion of 82 GPS measurements (described in detail in Section 3), which is similar in magnitude and distribution to the model of Moreno et al. (2012).

2. GPS data

Following the Maule earthquake, a dense network of 67 cGPS stations (Table S1, Figs. 1, S1b) was deployed and maintained in a multinational effort (Bevis et al., 2010; Vigny et al., 2011). Data for all stations were organized in 24 h periods. Each observation was processed using the Bernese GPS Software (Dach et al., 2007). Precise orbit and earth rotation parameters were used from IGS
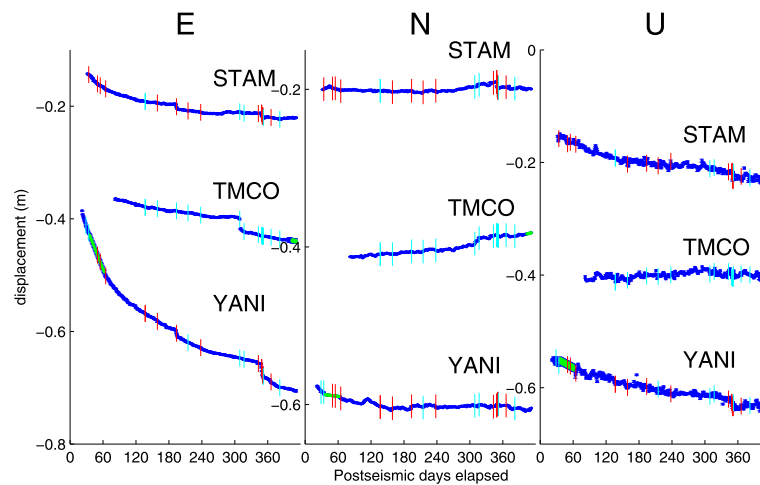
Fig. 2. East, North, and Vertical components of the continuous GPS data for 3 stations. Blue time series points correspond to real data, and green points correspond to linearly interpolated data. Interpolated data has been given an error 3 times that of the average, so that it is weighted less in model. Vertical red lines indicate plate interface aftershocks with Mw ⩾ 5.5 (from catalogue of Agurto et al., 2012) which have occurred within a lateral radius of 1°, and vertical cyan lines indicate earthquakes that have occurred further away. Aftershocks are often seen to line up with jumps and subsequent accelerations in the time series. (For interpretation of the references to colour in this figure, the reader is referred to the web version of this article.)

final products (Dow et al., 2009). During the processing, the antenna phase centre was reduced using absolute calibration, and double differences were modelled in L3, using elevation masks of 10° and a sampling rate of 30 s. To form the single differences a phase strategy of maximum observations was used. No a-priori troposphere model was applied. The troposphere parameters were estimated in all steps of parameter estimation. Corrections of the troposphere zenith delay for each station were estimated every 2 h. We used a Neill mapping function to compute the correction in the wet and dry part. The elevation-dependent weighting was applied using the function $\cos(z)^2$. We stacked the free solutions in a normal equation file for each day. For the datum definition we used the minimum constraint approach, applying the No Net Rotation (NNR) and No Net Translation (NNT) conditions for a group of selected reference stations (Table S2). Coordinates for each reference station were obtained from the global polyhedron weekly solution (Dow et al., 2009). Our results are compatible with ITRF2005 (Altamimi et al., 2007).

The post-seismic signal after the Maule earthquake is evident by high rate trench-ward (westward) movements and by the rapid decrease in the deformation rate (Fig. 2). We also see long and short period transient behaviour in the post-seismic signal, for example Fig. 2 shows peculiar accelerations in the North component of station YANI beginning at around post-seismic day 100. Sharp accelerations are usually related to large or nearby aftershocks (red lines on Fig. 2) and punctuate the decaying time series with step like features. The cGPS displacements for all stations can be found in the Supplementary Material (Table S1 and Fig. S1).

3. Kinematic modelling

3.1. Afterslip

Afterslip is modelled as along strike and up-dip dislocations on 1344 triangular patches with an average patch size of 180 km², using Green's functions of dislocations in an elastic halfspace (Okada, 1992). Rake is not constrained in the afterslip model, i.e. backslip is allowed to occur. The patches recreate the undulating plate interface, as modelled from gravity and seismicity by Tassara and Echaurren (2012), and extend from the trench to a depth of 100 km. The medium below the Earth's surface is modelled as a perfectly elastic, homogeneous halfspace with a typical subduction zone shear modulus of 35 GPa and a Poisson's ratio of 0.25

(Poisson's ratio is based on the average Vp/Vs value in the local earthquake tomography study of Haberland et al., 2009).

Spatio-temporal models of post-seismic afterslip in other studies have been created using either the Network Inversion Filter (NIF) (Segall and Matthews, 1997) or the Principal Components Analysis Method (PCAIM) (Kositsky and Avouac, 2010). To maximize the amount of data constraining our model, we split the data into non-overlapping 10 d periods (with a couple of exceptions; see Table S1), performed PCAIM on each period, before recombining the 10 d models to produce the total spatio-temporal model. This approach was necessary due to the significant gaps in the data; while PCAIM can handle small data gaps (Kositsky, 2010), for our model it was unable to produce reasonable results with too much missing data. To ensure a reasonable fit to the overall deformation at each station we interpolated data gaps linearly, but with the interpolated data weighted much less in the inversion than the real data (comparison of model with and without the interpolated data can be seen in Supplementary Material Figs. S1a, S3). At two stations (MOCH and SOLD), we made special interpolations to guide the model predictions along a reasonable deformation field (Fig. S1a). This was because we have data missing from both before and after the large Mw = 7.1 aftershock of January 2nd 2011. At these two nearby stations we interpolated both forwards and backwards to the date of the aftershock and inferred the jump in the interpolated time series to be the displacement from the aftershock. Slip was regularized by a Laplacian smoothing operator, and the weight of the smoothing operator was chosen at the elbow of the L-curve between misfit and roughness. Edge effects from the smoothing were reduced by implementing a border of patches surrounding the 1344 interface patches, on which the slip was constrained to be zero. The border of patches extends all edges of the plate interface (even the trench), and is neglected in all plots because it does not physically exist.

On March 11th 2010, there were two large aftershocks (Mw = 6.9 and Mw = 7.0) on crustal faults close to Pichilemu (Ryder et al., 2012; Farías et al., 2011). Since we did not want to contaminate the interface model with these clearly crustal events and their immediate afterslip, we did not invert for afterslip between 10th–12th March. The afterslip model does include the afterslip between 10th–12th March, however we set the afterslip for this period to be zero everywhere on the interface. Therefore the predicted displacements for this period are also zero at all stations. For comparison of data and predictions we do not consider this
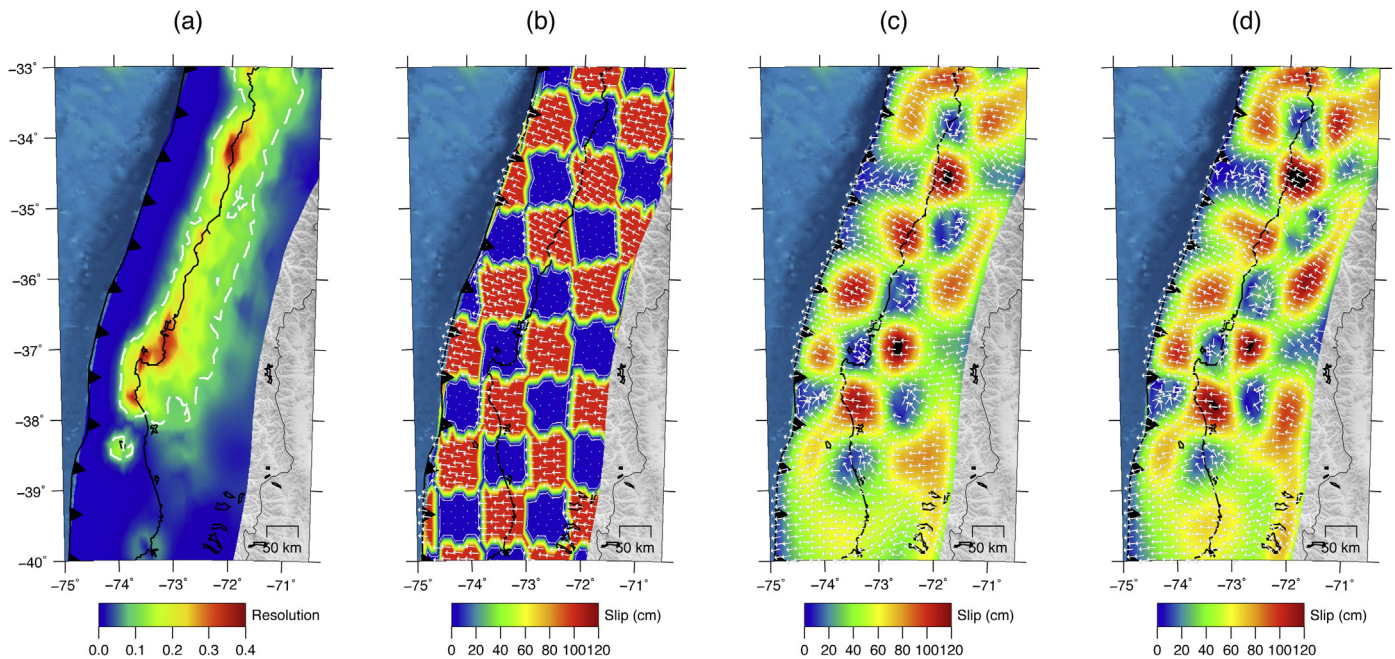
Fig. 3. (a) The diagonal of the model resolution matrix, averaged for both up-dip and along-strike model parameters, and averaged over all the inversions that are summed to produce the model. Model resolution matrix, R, is equal to $(G^{T}G)^{-1}G^{T}G$, where G is the matrix of Green's functions relating the dislocations in the elastic halfspace to the surface displacements (Menke, 1989). Higher values indicate better model resolution. The white dashed line encloses the region of the interface with superior resolution (resolution >0.1). (b) The input slip for the checkerboard test. Unit slip is implemented up-dip. (c) The inverted slip for the checkerboard test, using the synthetic displacements (without noise) 60 most commonly available cGPS stations. (d) The inverted slip for the checkerboard test, using the synthetic displacements (with noise) 60 most commonly available cGPS stations. Random uniformly distributed noise is added to each synthetic displacement, with the maximum noise being ±20% of the maximum displacement.

period, and in the data time series the GPS positions are shown as constant for days March 10th, 11th, and 12th.

The PCAIM modelling generates daily afterslip solutions (see the Supplementary Material Section S1 for more details of this method). However, this is not to say that the temporal resolution of the model is one day; since the signal to noise ratio in the data is decreasing in time (proportionally to the decay in surface GPS velocities) the daily afterslip solution accordingly becomes more noise dominated with time. For example, a two day period of the model early on in the post-seismic contains much more signal than a two day period later in the model.

3.2. Co-seismic slip

The co-seismic slip model was made using the same plate interface (including border) and regularization parameters as the post-seismic model. Vertical and horizontal displacements from 82 cGPS stations (Fig. S2) were inverted between 26th–27th February 2010, to produce the slip distribution of the megathrust earthquake. In addition to the published displacements (for processing details see Vigny et al., 2011) we used more solutions for the day before and during the earthquake (February 26th and 27th 2010) which were processed as described in Section 2.

3.3. Model resolution – what can we believe?

As is the case with any inversion model, certain model parameters are better constrained than others. Fig. 3a shows the diagonal elements of the model resolution matrix (Menke, 1989). The best resolution is obtained on the interface closest to the stations, and these are the areas of our slip model that we can have the most confidence in. A checkerboard test (where one forward models the displacement field of a checkerboard slip pattern on the interface and then inverts for slip using the available station distribution (e.g. Page et al., 2009), is a useful way to visualize limitations of

our method in resolving afterslip. Figs. 3c–d show the inversions of noise-free and noisy synthetic data generated by a checkerboard slip on the plate interface. The resolution is best near the coastline where the ~80 km wide checkerboards are clearly resolved along the whole strike extent of the Maule rupture zone. The up-dip patches near the trench (extending to a depth of around 15 km) are not resolvable (Fig. 3a) due to their location far outside the network. On the landward side, good resolution extends about 60–70 km east of the coastline. However, the poorly resolved area in the east corresponds to slab depths of more than 60 km. A threshold of 0.1 for the resolution matrix value, based on the inspection of checkerboard tests, has been chosen to separate regions with high and low resolution (white line, Fig. 3a).

4. Results

Fig. 4 shows the cumulative afterslip of the spatio-temporal model 420 d after the mainshock along with selected predicted and observed time series (all observed and predicted time series can be found in Fig. S1a; an animated sequence is shown in Animation S1). The model fits the data well in most stations; however at some stations, particularly in the volcanic arc, we observe a divergence of the predicted time series from the observed time series, where the stations see more deformation than we can model.

Within the extent of co-seismic rupture, we see high afterslip regions elongated along strike, ocean-side of the coast between 36.5° and 34°S, and high afterslip regions south of the Arauco Peninsula towards the southern termination of the co-seismic rupture area (Fig. 4). The elongated afterslip bands north of the Arauco peninsula seem to have two main patches (at 34.5° and 36°S), but the one at 34.5°S might also be influenced by the Pichilemu cluster of seismicity (Ryder et al., 2012). The densest cluster of the deep seismicity near 34.9°S and 71.8°W at approximately 50 km depth spatially coincides with cumulative afterslip of about 120 cm. The
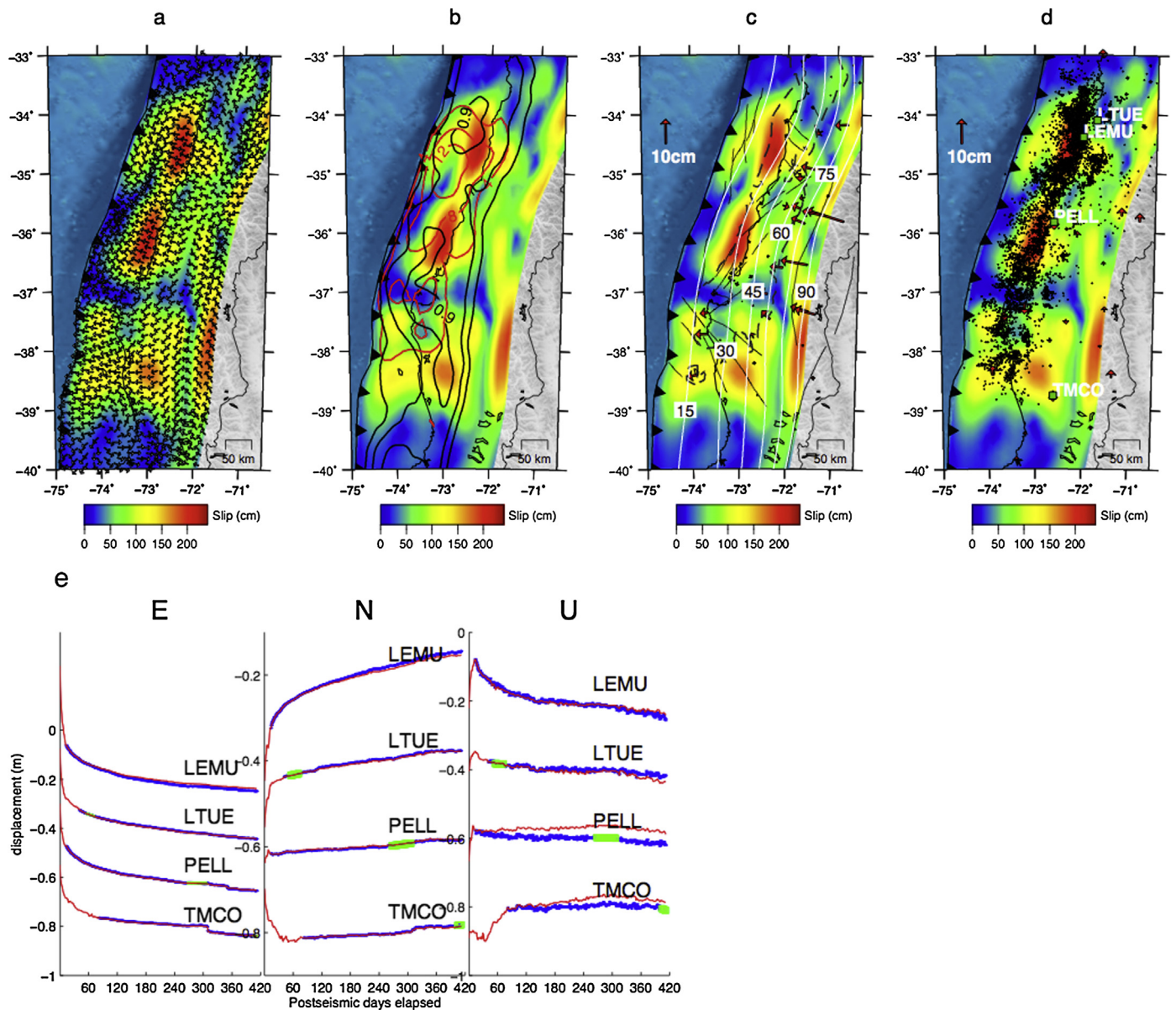
Fig. 4. (a) Cumulative afterslip between February 27th 2010 (day of mainshock) and April 15th 2011. Arrows show direction of slip on the interface. (b) Afterslip model overlain with the red mainshock slip contours (4, 8, and 12 m) and the black interseismic locking degree contours (0.3, 0.6, and 0.9) (Moreno et al., 2010). (c) Afterslip model and the horizontal misfit vectors (misfit = data – prediction). Misfits are plotted rather than the data and prediction vectors because the data at certain stations are incomplete for the model duration. Misfit is calculated between the first and last days of available data. White lines represent depth contours of the plate interface, spaced in 15 km intervals (slab model: Tassara and Echaurren, 2012). Black dashed line encloses the region of the interface with superior resolution (resolution >0.1). (d) Afterslip and the vertical misfit vectors. Black dots represent the aftershock seismicity from Lange et al. (2012). (e) Selected timeseries of model predictions and data. Blue, green, and red points represent the data, interpolated data, and the model predictions respectively. (For interpretation of the references to colour in this figure, the reader is referred to the web version of this article.)

high afterslip patch of around 170 cm at 38.3°S, 73°W lies in a region of poor resolution. There are regions of low afterslip at the Arauco Peninsula and land-side of the coast at 35.3°S. We see low to moderate afterslip down-dip towards the lower limits of the seismogenic zone, with local minima at 37° and 34°S. Afterslip is also low or even backslip is seen along most of the interface near the trench, but we must be aware that the resolution is very poor at the trench and the results of the checkerboard test suggest that we are unlikely to recover even broad slip distributions here (Fig. 3). Down-dip of the co-seismic rupture we see apparently very high afterslip in the deepest parts of the model.

Compared to the co- and post-seismic models of other well observed megathrusts, the Maule earthquake behaves somewhat similarly to the Tohoku Mw = 9.0, Japan 2011 (Ozawa et al., 2011) in that the afterslip mainly occurs down-dip of the mainshock peak

slip. However, the drop off in resolution towards the trench means that we cannot rule out that high afterslip of the Maule event has occurred in the up-dip regions. As is seen for the Tokachi-Oki Mw = 8.3, Japan 2003 (Miyazaki et al., 2004) and the Nias Mw = 8.7, Sumatra 2005 (Hsu et al., 2006), high afterslip tends to occur outside the regions of peak co-seismic slip (Fig. 4b) with the exception of the northernmost high afterslip region.

5. Discussion

5.1. Transient afterslip features

The primary motivation to produce a spatio-temporal model of afterslip was to test different modes of spatio-temporal variability (for example pulsing) against stationarity of the afterslip pattern
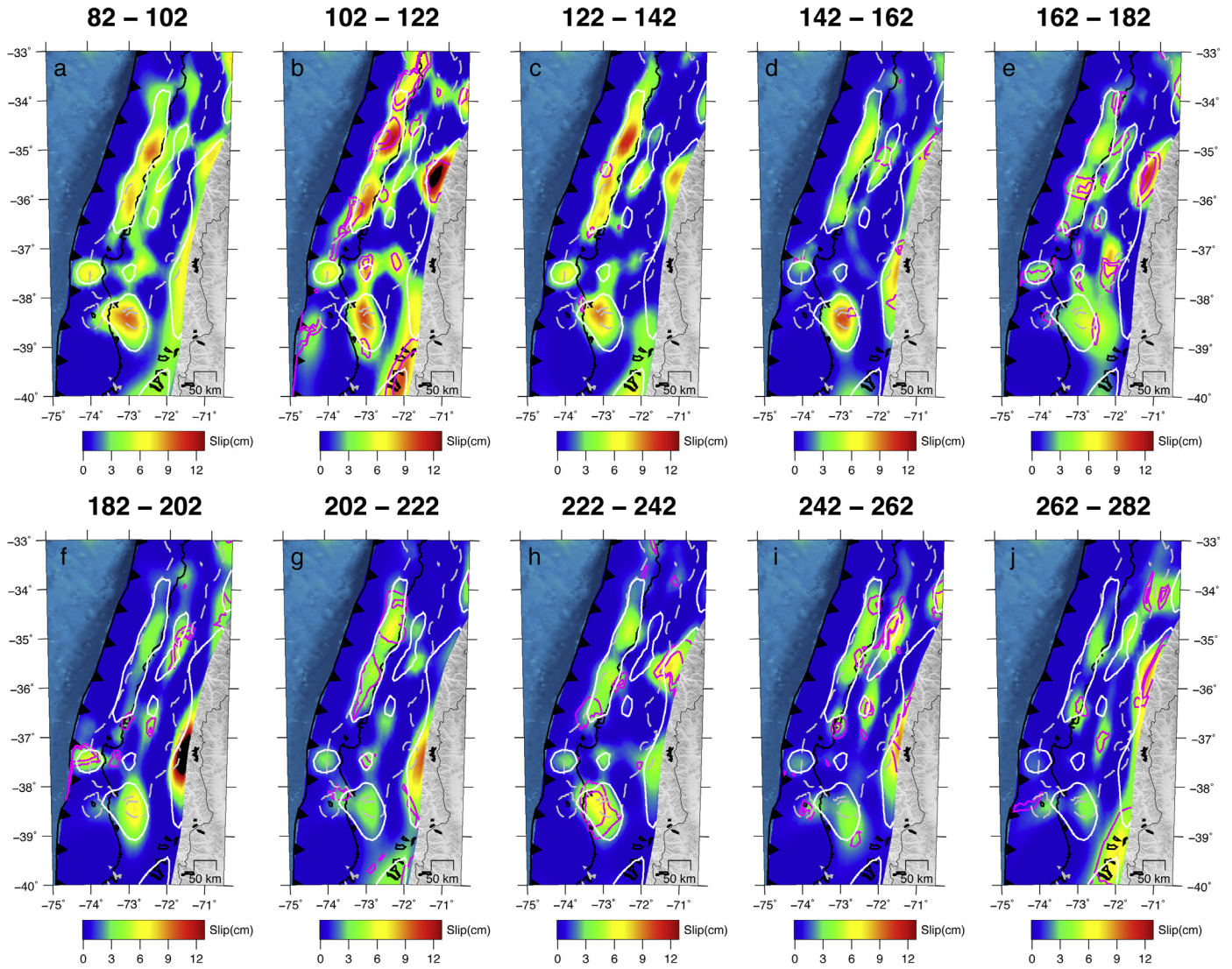
Fig. 5. The panels (a)–(j) represent 20 day time windows of up-dip afterslip as averaged from the jackknife testing between days 82–282 of the post-seismic period. Pink contours indicate robustly identified pulses of afterslip, with the first contour representing the ratio (slip difference: standard deviation) of 1:1 and the second contour a ratio of 2:1. There are no contours on panel a because this is the first time window of the analysis. White contour represents the 25 cm contour of up-dip afterslip between post-seismic days 82–282. Light grey dashed contour encloses the region of the interface with superior resolution (resolution >0.1). (For interpretation of the references to colour in this figure, the reader is referred to the web version of this article.)

shown in other studies and to characterize the transient nature of slip accumulation in detail. In order to minimize artificial variability due to time-variable GPS availability we restricted our investigation of afterslip variability to the period between post-seismic days 82–292 during which the model relies on 58 common stations. Fig. 5 shows how the afterslip varies in consecutive 20 d time windows. One might argue that any variability seen in the afterslip model is mainly due to noise in the GPS. To test this possibility we performed a jackknife test in which the individual 10 d inversions were repeated with a varying station distribution to gather a variety of models. Each 10 d time window was inverted 10 times, and each inversion used 52 random stations from the 58 available. By taking the mean of the inversions (for each time window) we can reveal which features of the model are most stable (i.e. most prevalent) in all of the solutions. This analysis works on the assumption that the noise for most station combinations is very weakly correlated in time. When the difference in mean slip of consecutive time windows is greater than the sum of the standard deviations of the consecutive time windows we can consider the difference in slip for the consecutive windows as being

robust. Due to the decaying nature of most time series we expect to see a decrease in slip with time. However, what we actually see are accelerations of slip (pulses) in various places within the regions releasing the most afterslip. Areas of pulsing for consecutive time windows are shown with contours in Fig. 5, along with a measure of robustness which is given by taking the ratio of slip difference to the sum of the standard deviations (1:1 is the minimum ratio for a pulse to be shown). Note that we only consider the up-dip component of the afterslip model since the regions of best resolution in the cumulative model exhibit predominantly up-dip slip. As discussed in Section 3.1, the signal to noise ratio will generally decay with time, so that the final 20 d window will be considerably more noise dominated than the first 20 d window. Therefore we also investigated the slip variability with each time window releasing the same moment in the shallowest 50 km of the plate interface, so that each time window should contain a similar amount of noise. Supplementary Fig. S4 demonstrates that for equal moment releases (each roughly equivalent to a seismic moment of Mw = 7.0) we also have considerable variation of afterslip pattern.

5.2. Misfit and slip vectors – secondary processes in action?

Although the model fits the data fairly well, and reproduces the transient signals within the post-seismic decay, it also produces considerable divergences between the observed and modelled cGPS time series at some stations. A plausible explanation for the divergence of fit could be viscoelastic relaxation of stress induced by the mainshock and poro-elastic rebound, both processes that are neglected in our model. Hu and Wang (2012) present similar misfit divergences from their model that simulates the post-seismic GPS data following the 2004 Sumatra megathrust, and achieve the best fit when they include both afterslip and viscoelastic stress relaxation. However, the fact that we do not see a long wavelength spatially coherent pattern in the magnitude of misfit (as would be expected by viscoelastic relaxation and poro-elastic rebound which induce coherent long wave length deformation at the surface) suggests that certain regions of the surface could also be affected by local processes such as crustal faulting or gravitational mass movement (e.g. landslides). Crustal faulting in the overriding plate is a particularly likely candidate to explain the juxtaposition of vertical motion between Mocha Island and stations on the coast. Furthermore, large variations in magnitude and orientation of the misfit (Fig. 4c, d) in post-seismic decay at stations which are very close together make it difficult to fit the time series with such a simple plate interface model.

Further hints that crustal fault motions are contributing to the surface deformation field come from the slip vectors. The slip vectors (Fig. 4a) are generally showing the continental plate moving towards the trench, especially at regions of high afterslip and in regions of better resolution. However, there are some counter-intuitive slip directions, albeit in poorly resolved regions of the interface. Interestingly, when we constrain the rake of the slip to be up-dip, the overall slip distribution patterns of free and constrained rake are comparable in areas of better model resolution (Fig. S3); however, slip is much more concentrated and absolute slip values in the model with the constrained rake are smaller by a factor of about two. As could be expected, the misfit of the model with constrained rake is much larger than for that with unconstrained rake, demonstrating that rake variations are necessary to fit the data. The most striking difference between both models occurs in the poorly resolved near-trench region in the northernmost part of the rupture. In the constrained-rake model no afterslip is inferred for this region, whereas for the unconstrained-rake model highly oblique slip with a significant backslip component is seen.

Other non-trench-ward motions can be seen down-dip of the mainshock area, possibly due to crustal fault motion which is neglected in our model and would be projected onto the deep plate interface. Accordingly, there have been several strike slip events in the volcanic arc (Agurto et al., 2012), such as the recent strike slip event (Mw = 6.0) occurring at ∼10 km depth on 7th June 2012. However, we must be cautious with our interpretations in regions of the model with such poor resolution (Fig. 3). Also we expect the assumptions of our simple model of plate interface afterslip to break down as we pass the continental Moho.

Slip in the well resolved regions of the interface is predominantly in the up-dip direction, corresponding to the roughly trench-normal GPS vectors (Animation S1), and not opposite to the plate convergence direction as one might expect from a release of accumulated strain on the plate interface. The reason for this up-dip slip direction is not clear and will be investigated in future work.

5.3. Relation between aftershocks and Coulomb stress changes

Agurto et al. (2012) show how the larger magnitude plate interface aftershocks for this megathrust have occurred at the fringes of the co-seismic slip distribution (Fig. 6a). This result is useful in terms of hazard assessment for identifying regions which are more likely to sustain larger aftershocks. However, it remains unclear by which mechanism these regions of the interface are triggered during the post-seismic phase, and why the larger aftershocks do not completely surround the co-seismic slip. If we assume the locations of aftershocks are controlled by static stress transfer expressed by a positive change of Coulomb Failure Stress (∆CFS) (e.g. King et al., 1994) then this raises the question as to whether the post-seismic afterslip is providing the additional static stress transfer to trigger these delayed aftershocks. The ∆CFS is calculated from the changes of the stress tensor with

$$\Delta CFS = \sigma_s - \sigma_n.\mu \qquad (1)$$

where μ is the coefficient of friction, σ_s is the change in shear stress (positive in up-dip direction) and σ_n is the change in normal stress (compression positive). According to the definition of ∆CFS the interface is brought closer to failure when ∆CFS is positive. The assumed failure direction needed for the shear component of the ∆CFS calculation was given by the up-dip direction for each patch of the model. Furthermore, we tested the sensitivity of the ∆CFS analysis results to the assumption of failure direction and it was found that within the range of failure directions captured by seismic centroid moment tensor (CMT) solutions the main findings of the analysis are unchanged (see Supplementary Material Section S2 and Figs. S5–S7 for more details).

Using the cumulative slip distribution from the mainshock and the time-varying post-seismic model (so that stress change is calculated only from slip preceding any particular aftershock) we calculated ∆CFS for each aftershock in the catalogues of Agurto et al. (2012) and Lange et al. (2012). We combined these two catalogues (excluding redundant events) because the Lange et al. (2012) catalogue includes lower magnitude events but only spans post-seismic days 14–214, whereas the Agurto et al. catalogue has a larger magnitude cut-off but spans all the post-seismic days of our afterslip model. We also included the Mw = 7.2 event of March 25th 2012, even though this takes place almost one year after the termination of our afterslip model. The traction on the plate interface (needed for ∆CFS) is calculated from the displacement gradient in the lithosphere. The displacement gradient is calculated from analytical solutions of dislocations in an elastic halfspace (Okada, 1992) using the same elastic parameters for the halfspace as used in the inversion models. We chose a homogeneous effective coefficient of friction $\mu = 0.1$ (Lamb, 2006). We tested the sensitivity of the calculations to changes in friction coefficient and found no qualitative impact.

Fig. 6 shows the ∆CFS distribution (including both normal and shear components) and its relationship to the co-seismic slip, afterslip, and the aftershocks. Clearly, most of the lower magnitude events occur in areas of negative ∆CFS (Fig. 6e; see Fig. S6 for a histogram of ∆CFS at the hypocentres and origin times of the earthquakes) and therefore static stress transfer does not seem to be the physical mechanism triggering these aftershocks. At the larger magnitudes (for example Mw > 5) although less data points are available, a tendency for the aftershocks to lie in the areas of negative ∆CFS seems to be the result (Figs. 6, S6). However, we must consider the effect of smoothing of the co-seismic inversion – it is likely that the larger magnitude events (shown as white circles in Fig. 6) are lying in positively stressed parts of the plate interface which are smeared over with negative ∆CFS from the smoothing. Two of the three plate interface aftershocks with Mw > 6.8 occur in regions of positive Coulomb stress but as all three events occur in areas of large ∆CFS gradients, minor uncertainties in slip model or epicentral location could mean that all occurred in positive ∆CFS regions.
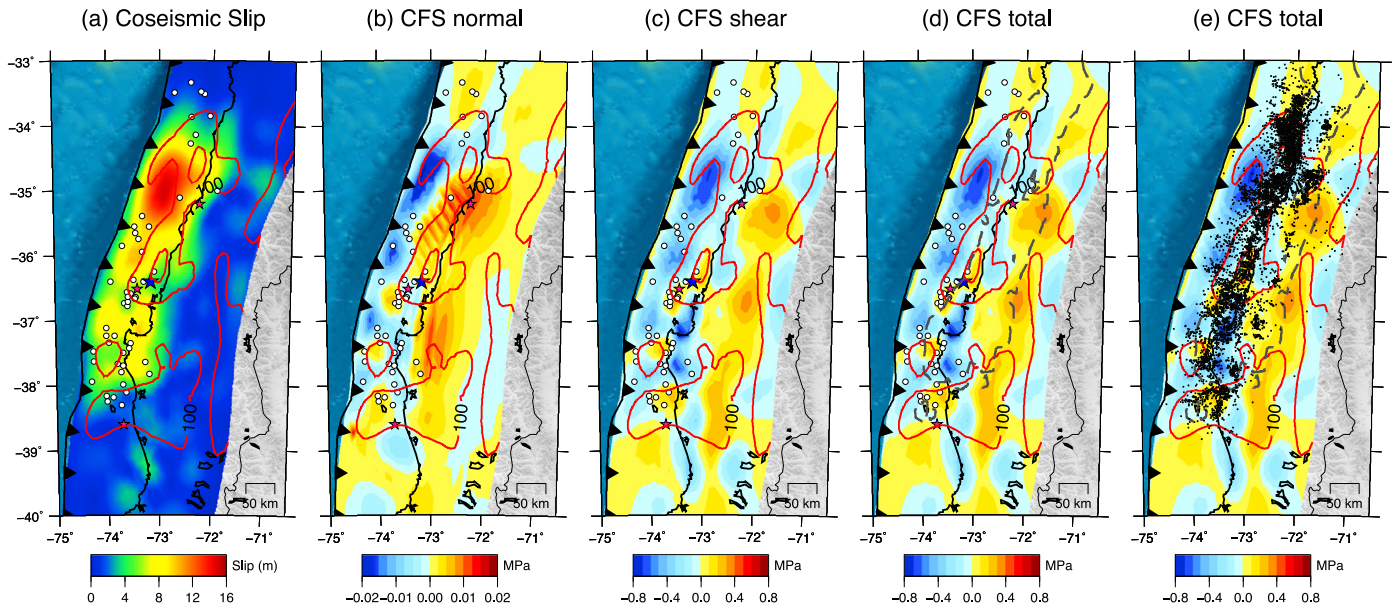
Fig. 6. (a) Co-seismic slip. White circles are the plate interface thrust events larger than Mw = 5.5, pink stars are the largest aftershocks on the plate interface (from north to south Mw = 7.2, 6.8, 7.1), and the blue star is the epicentre of the mainshock (hypocentre from Vigny et al., 2011. All other epicentres from Agurto et al., 2012). Red contours represent 100 cm and 200 cm of afterslip (in any direction). (b) Normal component of the ΔCFS calculation assuming a coefficient of friction mu = 0.1. Positive indicates a change in stress bringing the interface closer to failure. The circles, stars, and red contours indicate the same things stated for panel (a). (c) Shear component (in up-dip direction) of the ΔCFS calculation. Positive indicates a change in stress bringing the interface closer to failure. The circles, stars, and red contours indicate the same things stated for panels (a)–(b). (d) Total ΔCFS. Positive indicates a change in stress bringing the interface closer to failure. The circles, stars, and red contours indicate the same things stated for panels (a)–(c). The grey dashed line encloses the region of the interface with superior resolution (resolution >0.1). (e) Total ΔCFS. Black dots represent the plate interface seismicity (events which are ±5 km from the plate interface as defined by Tassara and Echaurren (2012). Seismicity from the catalogue of Lange et al. (2012). The red contours indicate the same things stated for panels (a)–(d). The grey dashed line encloses the region of the interface with superior resolution (resolution >0.1). (For interpretation of the references to colour in this figure, the reader is referred to the web version of this article.)

Black contours in Fig. 6d show high afterslip (>200 cm) in regions of positive co-seismic ΔCFS for the well resolved regions south–west of the Arauco Peninsula and south of the hypocentre. Conversely, high afterslip (>200 cm) in the well resolved region north of the hypocentre (at around −34.6°S–72.3°W) coincides with a stress shadow (region of negative ΔCFS). It is intriguing as to why we observe the highest afterslip values in the stress shadow; one possible explanation is that this region has undergone a significant increase in pore fluid pressure to lithostatic or even supralithostatic levels following the mainshock. Such a mechanism might cause a large enough drop in effective normal stress allowing high afterslip in the presence of very low shear stresses. Alternatively, the initial (pre-mainshock) stress conditions of this region could be the reason for high afterslip: As the ΔCFS calculation only takes into account the change in stress due to the mainshock and afterslip, afterslip might well release high shear stresses built up during the interseismic period preceding the mainshock. In that case a spatial correlation between afterslip and preseismic locking should be present. From Fig. 4b we see that regions of high afterslip (>150 cm) overlap considerably with areas of high locking (>0.9) and only moderate co-seismic slip (<10 m) suggesting that relaxation of incomplete stress drops from the co-seismic rupture as a dominant mechanism driving afterslip.

5.4. Implications for mechanics of the subduction interface

Since we now have preseismic geodetic locking, co-seismic slip and afterslip models for the Maule event we can study this megathrust in terms of the pre-, co-, and post-seismic phases of the earthquake cycle, and speculate on the physical properties and stress field conditions that govern the kinematic and dynamic interface behaviour. The plate interface at regions of great subduction zone earthquakes is often thought to consist of interfingering areas of contrasting frictional properties, which are ultimately controlling the feedback of pre-, co- and post-seismic

processes (Kanamori and Brodsky, 2001). The asperity model (Lay and Kanamori, 1981) describes the subduction interface as consisting of asperities which build up stress inter-seismically and fail suddenly while the surrounding interface creeps. The development of rate and state friction laws over the past decades (e.g. Scholz, 1998) describes how such asperity and creeping zones should behave when critically stressed (i.e. when a rupture front propagates into the zone). In rate-weakening zones, the frictional strength will decrease when slip rate increases leading to instability and increasing the likelihood of continued rupture propagation. Zones of rate-strengthening friction behave in the opposite manner, increasing the friction during accelerated slip and strongly counteracting rupture propagation. It has often been assumed that the geodetically highly locked regions are acting as asperities and correspond to the rate-weakening friction zones, whereas the creeping regions correspond to rate-strengthening friction zones. However, this simplistic binary view is inconsistent with observations of post-seismic creep on supposed asperities following the great Tohoku-Oki megathrust of 2011 (Johnson et al., 2012).

In order to analyse the frictional behaviour in more detail, we compared afterslip to slip from aftershocks by calculating the *post-seismic seismic efficiency* (*PSE*) (Tilmann et al., 2010); i.e. the percentage of slip which is released seismically during the post-seismic observation period. By forward modelling the expected slip and rupture area from scaling relationships (Wells and Coppersmith, 1994) for aftershock events that occurred on the plate interface during the time period of our afterslip model (Agurto et al., 2012) then inverting the displacement field using our time varying station coverage, we produced an approximation of the seismic contribution to the cumulative afterslip model (i.e. the seismic coupling coefficient during accelerated slip) and hence we quantified the percentage of seismic slip captured in our model. The slip in the forward modelling is assumed to be in the local up-dip direction and is performed on a finer mesh with an av-
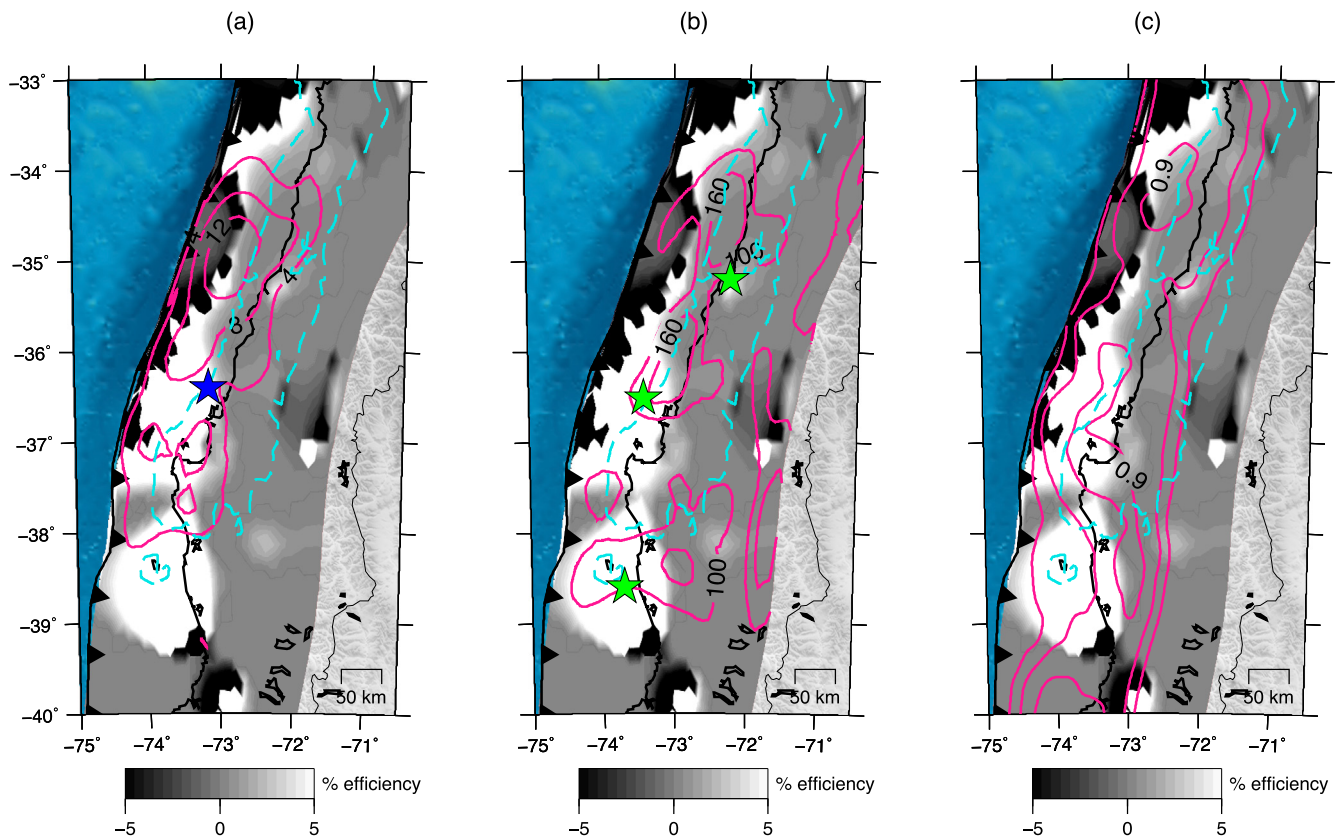
Fig. 7. (a) Post-seismic Seismic Efficiency (PSE) with magenta contours of co-seismic slip (4, 8, and 12 m). Blue star is the mainshock hypocentre (Vigny et al., 2011). The blue dashed line encloses the region of the interface with superior resolution (resolution >0.1). (b) PSE with magenta contours of afterslip (100 and 160 cm). Green stars are the largest aftershocks on the plate interface (pink stars in Fig. 6). The large aftershock at 35.2°S happens over one year later – it is not included in the calculation of PSE. The blue dashed line encloses the region of the interface with superior resolution (resolution >0.1). (c) PSE with contours of interseismic locking degree (contour intervals: 0.3, 0.6, and 0.9). The blue dashed line encloses the region of the interface with superior resolution (resolution >0.1). (For interpretation of the references to colour in this figure, the reader is referred to the web version of this article.)

erage patch area of 11 km^2. The forward modelled slip for each earthquake is consistent with the equation for seismic moment:

$$M_o = SD \sum_j A_j$$

where S is the shear modulus of the faulted material, A_j is the area of each patch in the rupture area, and D is the average slip on the rupture. First we selected a suitable source area for each aftershock by selecting the closest patch(es) to the hypocentre. The number of patches was determined by the minimum misfit between theoretical rupture area and cumulative area of patches. Then we adjusted the slip to satisfy the moment according to Eq. (2). For lower magnitude events the rupture areas are unrealistically large with very low values of slip which, even in such high frequency, have a negligible effect on the surface displacement field. Therefore we only consider the largest plate interface aftershocks as presented in the paper of Agurto et al. (2012). Inversion of the synthetic data is performed using the same regularization and model parameters that were used in the afterslip inversion. PSE appears to be negative in regions where we have backslip in the cumulative afterslip model but this only appears in poorly resolved regions of the plate interface, allowing us to disregard the negative regions in the subsequent discussion.

In general PSE is relatively low (<10% for most areas), although we must consider that the seismic slip is smeared during both the forward modelling and the regularization of the inversion. In reality PSE values are likely to be larger, and so values of PSE should only be interpreted relatively. Furthermore, the smearing of the inversion puts seismic slip onto regions of the interface which may

in reality have very little seismicity, and this effect is exacerbated with larger events. Nevertheless, this method is useful for showing differences in mode of afterslip release over broad spatial scales.

Figs. 7a–c show the PSE (clipped at 5% for clarity) versus the co-seismic slip, afterslip and interseismic locking distributions. There seems to be no obvious correlation between co-seismic slip and PSE (Fig. 7a) although we see high PSE together with moderately high co-seismic slip at the Arauco Peninsula (a region where the co-seismic model also has good resolution due to good station coverage; see Fig. S2). Also in this region we see high interseismic coupling. From Fig. 7b we see that most regions of high afterslip are aseismic with the exception of the region near Mocha Island, where the Mw = 7.1 occurred on January 2nd 2011.

Under rate-and-state physics, the more highly seismically efficient regions of the plate interface should correspond to the rate-weakening zones because the stress is being released more suddenly. Therefore it seems that the Arauco peninsula is behaving as a rate-weakening asperity which becomes highly locked in the interseismic, releases large slip co-seismically, and has a relatively high PSE to surrounding regions. Heading North along the coastline there seems to be a transition from a rate-weakening into a rate-strengthening region with peak afterslip centred at 73°W 36.2°S, and this transition in from high to low PSE coincides with the termination of a very highly preseismically locked slither (Fig. 7c). This region has undergone a strong increase in ∆CFS due to the mainshock (Fig. 6d) yet it releases this stress with predominantly aseismic afterslip and was locked to a lesser degree (i.e. creeping more) than the Arauco peninsula during the interseismic. The gradual release of mainly aseismic slip centred at 73°W 36.2°S is

of stark contrast to the also positive ΔCFS region nearby to the southwest at 73.6°W 36.7°S (Fig. 6d) which releases stress with some of the largest plate interface aftershocks. As the high afterslip region extends Northwards along the coast towards 34°S it becomes less straightforward to characterize the frictional properties of the plate interface. As discussed in Section 5.3, we see high afterslip in a region with a negative ΔCFS which could be due to a slip-deficit, expulsion of fluids onto the interface, or a combination of both these effects. This region of low PSE afterslip lies in an area of high co-seismic slip (>8 m) – a colocation that we would not expect if this region behaved with purely rate-weakening mechanics. From the low PSE one might be inclined to say this is a rate-strengthening region, however this seems incompatible with the high afterslip at regions of very high interseismic locking. In the context of conditional stability this behaviour can only be reconciled by assuming that pore pressures increased at these locations during or shortly after the mainshocks. We therefore interpret the creep which we see on the supposed asperity as due to a transient elevation in pore fluid pressure. If an increase in fluids on the interface is facilitating the large afterslip of this region then perhaps it is also facilitating the high density of low magnitude events in this region.

Interestingly, anomalously high PSE compared to surrounding regions at 72.2°W 35.2°S coincides with the hypocentre of one of the largest plate interface aftershocks (Mw = 7.1) that occurred on March 25th 2012 (for PSE calculation we only used events until April 11th 2011).

6. Conclusions

The proximity of cGPS to the seismogenic plate interface and the excellent spatial coverage has allowed us to model the spatio-temporal changes of afterslip with unprecedented resolution. We have found that afterslip accumulates in pulses in specific regions on the plate interface, rather than decaying with a stationary pattern or migrating (Animation S1). While most of the afterslip is aseismic (Fig. 7), the plate interface aftershocks tend to line up over regions of high afterslip (Fig. 4d). We have shown that most of the plate interface aftershocks (which are of low magnitude) are not triggered by the transfer of co- and post-seismic static stresses, and from this result we can speculate on other possible mechanisms controlling aftershocks. If we assume that poro-elastic rebound and visco-elastic stress relaxation would only result in a long-wavelength pattern of the post-seismic GPS signals then these processes would also not explain the locations or decay of the aftershocks. Since our model captures most of the post-seismic signal we hypothesize that the processes that control the strength are mainly due to pore pressure diffusion due to pathways opened at the interface by the mainshock (e.g. Shapiro et al., 2003). This might result in significant decrease of the effective normal stress, i.e. an increase of positive ΔCFS. However, pore pressure changes (particularly when they occur locally) would not leave an imprint on the GPS signal. The hypothesis of pore pressure diffusion could also explain the high afterslip and pulsing behaviour, both for areas with positive and negative ΔCFS. Additionally, we have demonstrated that the simple rate-and-state friction based models to explain locking, asperities, co-seismic rupture and afterslip distribution do not seem to hold for this megathrust, with the Maule 2010 afterslip occurring in both highly preseismically locked zones and in zones of lower preseismic locking. Since both afterslip pulses and the majority of aftershocks are possibly both linked to fluid effects, a sensible next step would be to establish whether a spatio-temporal relation exists between afterslip pulses and aftershocks.

Footnote

At the time of re-submission of this article, an independent study of the co- and post-seismic slip for the Maule 2010 event (Lin et al., 2013) has been accepted for publication.

Appendix A. Supplementary material

Supplementary material related to this article can be found online at http://dx.doi.org/10.1016/j.epsl.2013.09.020.

References

Agurto, H., Rietbrock, A., Ryder, I., Miller, M., 2012. Seismic-afterslip characterization of the 2010 MW 8.8 Maule, Chile, earthquake based on moment tensor inversion. Geophys. Res. Lett. 39, L20303.

Allmendinger, R.W., Cardozo, N., Fisher, D., 2012. Structural Geology Algorithms: Vectors and Tensors in Structural Geology. Cambridge University Press.

Altamimi, Z., Collilieux, X., Legrand, J., Garayt, B., Boucher, C., 2007. ITRF2005: A new release of the International Terrestrial Reference Frame based on time series of station positions and Orientation Parameters. J. Geophys. Res. 112. 19 pp.

Bevis, M.G., Brooks, B.A., Smalley, R., Baez, J.C., Parra, H., Kendrick, E.C., Foster, J.H., Blanco, M., Simons, M., Caccamise, D., Genrich, J.F., Sladen, A., Melnick, D., Moreno, M., Cimbaro, S., Ryder, I.M., Wang, K., Bataille, K., Cassasa, G., Klotz, J., Folguera, A., Tong, X., Sandwell, D.T., 2010. The 2010 (M 8.8) Maule, Chile earthquake: an overview of the emergency geodetic response and some of its early findings (invited). In: AGU Fall Meeting Abstracts 1. 04.

Dach, R., Hugentobler, U., Fridez, P., Meindl, M., 2007. Bernese GPS Software Version 5.0. Astronomical Institute, University of Bern.

Darwin, C., 1851. Geological Observations on Coral Reefs, Volcanic Islands, and on South America: Being the Geology of the Voyage of the Beagle, under the Command of Captain Fitzroy, R.N., During the Years 1832 to 1836. Smith, Elder.

Delouis, B., Nocquet, J.-M., Vallée, M., 2010. Slip distribution of the February 27, 2010 Mw = 8.8 Maule Earthquake, central Chile, from static and high-rate GPS, InSAR, and broadband teleseismic data. Geophys. Res. Lett. 37. 7 pp.

Dow, J.M., Neilan, R.E., Rizos, C., 2009. The International GNSS Service in a changing landscape of Global Navigation Satellite Systems. J. Geod. 83, 191–198.

Farías, M., Comte, D., Roecker, S., Carrizo, D., Pardo, M., 2011. Crustal extensional faulting triggered by the 2010 Chilean earthquake: The Pichilemu Seismic Sequence. Tectonics 30. 11 pp.

Freed, A.M., Bürgmann, R., Calais, E., Freymueller, J., 2006. Stress-dependent power-law flow in the upper mantle following the 2002 Denali, Alaska, earthquake. Earth Planet. Sci. Lett. 252, 481–489.

Haberland, C., Rietbrock, A., Lange, D., Bataille, K., Dahm, T., 2009. Structure of the seismogenic zone of the southcentral Chilean margin revealed by local earthquake traveltime tomography. J. Geophys. Res. 114, B01317.

Helmstetter, A., Shaw, B.E., 2009. Afterslip and aftershocks in the rate-and-state friction law. J. Geophys. Res. 114. 24 pp.

Hergert, T., Heidbach, O., 2006. New insights in the mechanism of postseismic stress relaxation exemplified by the June 23rd 2001 Mw = 8.4 earthquake in southern Peru. Geophys. Res. Lett. 33, L02307, http://dx.doi.org/10.1029/2005GL024585.

Hsu, Y.-J., Simons, M., Avouac, J.-P., Galetzka, J., Sieh, K., Chlieh, M., Natawidjaja, D., Prawirodirdjo, L., Bock, Y., 2006. Frictional afterslip following the 2005 Nias-Simeulue earthquake, Sumatra. Science 312, 1921–1926.

Hsu, Y.-J., Segall, P., Yu, S.-B., Kuo, L.-C., Williams, C.A., 2007. Temporal and spatial variations of post-seismic deformation following the 1999 Chi–Chi, Taiwan earthquake. Geophys. J. Int. 169, 367–379.

Hu, Y., Wang, K., 2012. Spherical-Earth finite element model of short-term postseismic deformation following the 2004 Sumatra earthquake. J. Geophys. Res. 117. 15 pp.

Hu, Y., Wang, K., He, J., Klotz, J., Khazaradze, G., 2004. Three-dimensional viscoelastic finite element model for postseismic deformation of the great 1960 Chile earthquake. J. Geophys. Res. 109. 14 pp.

Hughes, K.L.H., Masterlark, T., Mooney, W.D., 2010. Poroelastic stress-triggering of the 2005 M8.7 Nias earthquake by the 2004 M9.2 Sumatra–Andaman earthquake. Earth Planet. Sci. Lett. 293, 289–299.

Johnson, K.M., Fukuda, J., Segall, P., 2012. Challenging the rate-state asperity model: Afterslip following the 2011 M9 Tohoku-oki, Japan, earthquake. Geophys. Res. Lett. 39, L20302.

Kanamori, H., Brodsky, E., 2001. The physics of earthquakes. Phys. Today 54, 34.

King, G.C.P., Stein, R.S., Lin, J., 1994. Static stress changes and the triggering of earthquakes. Bull. Seismol. Soc. Am. 84, 935–953.

Kiser, E., Ishii, M., 2011. The 2010 Mw 8.8 Chile earthquake: Triggering on multiple segments and frequency-dependent rupture behavior. Geophys. Res. Lett. 38, L07301, http://dx.doi.org/10.1029/2011GL047140.

Kositsky, A.P., 2010. PCAIM user's manual. http://www.tectonics.caltech.edu/resources/pcaim/pubs/pcaim_manual.pdf.

Kositsky, A.P., Avouac, J.-P., 2010. Inverting geodetic time series with a principal component analysis-based inversion method. J. Geophys. Res. 115. 19 pp.

Lamb, S., 2006. Shear stresses on megathrusts: Implications for mountain building behind subduction zones. J. Geophys. Res. 111 (B7), B07401.

Lange, D., Tilmann, F., Barrientos, S.E., Contreras-Reyes, E., Methe, P., Moreno, M., Heit, B., Agurto, H., Bernard, P., Vilotte, J.-P., Beck, S., 2012. Aftershock seismicity of the 27 February 2010 Mw 8.8 Maule earthquake rupture zone. Earth Planet. Sci. Lett. 317–318, 413–425.

Lay, T., Kanamori, H., 1981. An asperity model of large earthquake sequences. Maurice Ewing Ser. 4, 579–592.

Lin, Y.N., Sladen, A., Ortega-Culaciati, F., Simons, M., Avouac, J.-P., Fielding, E.J., Brooks, B.A., Bevis, M., Genrich, J., Rietbrock, A., Vigny, C., Smalley, R., Socquet, A., 2013. Coseismic and postseismic slip associated with the 2010 Maule Earthquake, Chile: Characterizing the Arauco Peninsula barrier effect. J. Geophys. Res., Solid Earth 118, 3142–3159.

Lorito, S., Romano, F., Atzori, S., Tong, X., Avallone, A., McCloskey, J., Cocco, M., Boschi, E., Piatanesi, A., 2011. Limited overlap between the seismic gap and coseismic slip of the great 2010 Chile earthquake. Nat. Geosci. 4, 173–177.

Marone, C., 1998. Laboratory-derived friction laws and their application to seismic faulting. Annu. Rev. Earth Planet. Sci. 26, 643–696.

Marone, C.J., Scholz, C.H., Bilham, R., 1991. On the mechanics of earthquake afterslip. J. Geophys. Res. 96 (B5), 8441–8452, http://dx.doi.org/10.1029/91JB00275.

Menke, W., 1989. Geophysical Data Analysis: Discrete Inverse Theory. Academic Press.

Métois, M., Socquet, A., Vigny, C., 2012. Interseismic coupling, segmentation and mechanical behavior of the central Chile subduction zone. J. Geophys. Res. 117, B03406.

Miyazaki, S., Segall, P., Fukuda, J., Kato, T., 2004. Space time distribution of afterslip following the 2003 Tokachi-oki earthquake: Implications for variations in fault zone frictional properties. Geophys. Res. Lett. 31. 4 pp.

Moreno, M., Rosenau, M., Oncken, O., 2010. 2010 Maule earthquake slip correlates with pre-seismic locking of Andean subduction zone. Nature 467, 198–202.

Moreno, M., Melnick, D., Rosenau, M., Baez, J., Klotz, J., Oncken, O., Tassara, A., Chen, J., Bataille, K., Bevis, M., Socquet, A., Bolte, J., Vigny, C., Brooks, B., Ryder, I., Grund, V., Smalley, B., Carrizo, D., Bartsch, M., Hase, H., 2012. Toward understanding tectonic control on the Mw 8.8 2010 Maule Chile earthquake. Earth Planet. Sci. Lett. 321–322, 152–165.

Okada, Y., 1992. Internal deformation due to shear and tensile faults in a half-space. Bull. Seismol. Soc. Am. 82, 1018–1040.

Ozawa, S., Nishimura, T., Suito, H., Kobayashi, T., Tobita, M., Imakiire, T., 2011. Coseismic and postseismic slip of the 2011 magnitude-9 Tohoku-Oki earthquake. Nature 475, 373–376.

Page, M.T., Custódio, S., Archuleta, R.J., Carlson, J.M., 2009. Constraining earthquake source inversions with GPS data: 1. Resolution-based removal of artifacts. J. Geophys. Res. 114. 13 pp.

Perfettini, H., Avouac, J.-P., Tavera, H., Kositsky, A., Nocquet, J.-M., Bondoux, F., Chlieh, M., Sladen, A., Audin, L., Farber, D.L., Soler, P., 2010. Seismic and aseismic slip on the Central Peru megathrust. Nature 465, 78–81.

Pollitz, F.F., Brooks, B., Tong, X., Bevis, M.G., Foster, J.H., Bürgmann Jr., R.S., Vigny, C., Socquet, A., Ruegg, J.-C., Campos, J., Barrientos, S., Parra, H., Soto, J.C.B., Cimbaro, S., Blanco, M., 2011. Coseismic slip distribution of the February 27, 2010 Mw 8.8 Maule, Chile earthquake. Geophys. Res. Lett. 38, 5 pp.

Rietbrock, A., Ryder, I., Hayes, G., Haberland, C., Comte, D., Roecker, S., Lyon-Caen, H., 2012. Aftershock seismicity of the 2010 Maule Mw = 8.8, Chile, earthquake: Correlation between co-seismic slip models and aftershock distribution?. Geophys. Res. Lett. 39. 5 pp.

Ruegg, J.C., Rudloff, A., Vigny, C., Madariaga, R., de Chabalier, J.B., Campos, J., Kausel, E., Barrientos, S., Dimitrov, D., 2009. Interseismic strain accumulation measured by GPS in the seismic gap between Constitución and Concepción in Chile. Phys. Earth Planet. Inter. 175, 78–85.

Rundle, J.B., 1978. Viscoelastic crustal deformation by finite quasi-static sources. J. Geophys. Res. 83 (B12), 5937–5945.

Ryder, I., Rietbrock, A., Kelson, K., Bürgmann, R., Floyd, M., Socquet, A., Vigny, C., Carrizo, D., 2012. Large extensional aftershocks in the continental forearc triggered by the 2010 Maule earthquake, Chile. Geophys. J. Int. 188, 879–890.

Scholz, C.H., 1998. Earthquakes and friction laws. Nature 391, 37–42.

Segall, P., Matthews, M., 1997. Time dependent inversion of geodetic data. J. Geophys. Res. 102, 22391.

Segall, P., Burgmann, R., Matthews, M., 2000. Time-dependent triggered afterslip following the 1989 Loma Prieta earthquake. J. Geophys. Res. 105 (B3), 5615–5634.

Shapiro, S.A., Patzig, R., Rothert, E., Rindschwentner, J., 2003. Triggering of seismicity by pore-pressure perturbations: Permeability-related signatures of the phenomenon. Pure Appl. Geophys. 160 (5), 1051–1066.

Tassara, A., Echaurren, A., 2012. Anatomy of the Andean subduction zone: three-dimensional density model upgraded and compared against global-scale models. Geophys. J. Int. 189 (1), 161–168.

Tilmann, F., Craig, T.J., Grevemeyer, I., Suwargadi, B., Kopp, H., Flueh, E., 2010. The updip seismic/aseismic transition of the Sumatra megathrust illuminated by aftershocks of the 2004 Aceh-Andaman and 2005 Nias events. Geophys. J. Int. 181, 1261–1274, http://dx.doi.org/10.1111/j.1365-246X.2010.04597.

Vigny, C., Socquet, A., Peyrat, S., Ruegg, J.-C., Métois, M., Madariaga, R., Morvan, S., Lancieri, M., Lacassin, R., Campos, J., Carrizo, D., Bejar-Pizarro, M., Barrientos, S., Armijo, R., Aranda, C., Valderas-Bermejo, M.-C., Ortega, I., Bondoux, F., Baize, S., Lyon-Caen, H., Pavez, A., Vilotte, J.P., Bevis, M., Brooks, B., Smalley, R., Parra, H., Baez, J.-C., Blanco, M., Cimbaro, S., Kendrick, E., 2011. The 2010 Mw 8.8 Maule megathrust earthquake of Central Chile, monitored by GPS. Science 332, 1417–1421.

Wang, D., Mori, J., 2011. Frequency-dependent energy radiation and fault coupling for the 2010 Mw 8.8 Maule, Chile, and 2011 Mw 9.0 Tohoku, Japan, earthquakes. Geophys. Res. Lett. 38. 6 pp.

Wang, H.F., 2000. Theory of Linear Poroelasticity with Applications to Geomechanics and Hydrogeology. Princeton University Press.

Wang, K., Hu, Y., He, J., 2012. Deformation cycles of subduction earthquakes in a viscoelastic Earth. Nature 484, 327–332.

Wells, D.L., Coppersmith, K.J., 1994. New empirical relationships among magnitude, rupture length, rupture width, rupture area, and surface displacement. Bull. Seismol. Soc. Am. 84, 974–1002.

Wessel, P., Smith, W.H., 1998. New, improved version of Generic Mapping Tools released. Eos 79 (47), 579.